LAWRENCE
LIVERMORE
NATIONAL
LABORATORY

A Geophysical Shock and Air Blast Simulator at the National Ignition Facility

K. B. Fournier, C. G. Brown, M. J. May, S. Compton, N. Shingleton, O. R. Walton, J. O. Kane, P. B. Mirkarimi, W. H. Dunlop, R. L. Guyton, E. Huffman

April 22, 2014

Disclaimer

A Geophysical Shock and Air Blast Simulator at the National Ignition Facility

Kevin B. Fournier, Charles G. Brown Jr., Mark J. May, Steven Compton, N. Shingleton, Otis R. Walton, Jave O. Kane, Paul B. Mirkarimi, William H. Dunlop[1] and Robert L. Guyton and Eric Huffman[2]

[1] *Lawrence Livermore National Laboratory, P.O. Box 808, L-481, Livermore, CA 94550, USA*

[2] *National Securities Technologies, Vasco Rd., Livermore, CA 94551, USA*

(Dated: 22 April 2014)

The Energy Partitioning Energy Coupling (EPEC) experiments at the National Ignition Facility (NIF) have been designed to simultaneously measure the coupling of energy into both ground shock and air-blast over-pressure from a laser-driven target to nearby media. The source target for the experiment is positioned at a known height above the ground-surface simulant and is heated by four beams from the NIF. The resulting target energy density and specific energy are equal to those of a low-yield nuclear device. The ground-shock stress waves and atmospheric overpressure waveforms that result in our test system are hydrodynamically scaled analogs of full-scale seismic and air-blast phenomena. This report summarizes the development of the platform, the simulations and calculations that underpin the physics measurements that are being made, and finally the data that were measured. Very good agreement is found for scaled arrival times, and agreement on the order of a factor of two is seen for other air-blast quantities. Historical underground test data for seismic phenomena measured sensor displacements; we measure the stresses generated in our ground-surrogate medium. We find factors-of-a-few agreement between our measured peak stresses and predictions with modern geophysical computer codes.

PACS numbers: tbd

I. INTRODUCTION

We report on the Energy Partitioning, Energy Coupling (EPEC) experiment at the National Ignition Facility (NIF)[1,2]. The EPEC experiment uses the NIF laser beams to create a high-energy-density source that drives blast waves in a test atmosphere and shock waves in a ground medium. This blast and shock simulator can be used to study the partitioning of the source energy into air blast and ground shock as a function of the height of burst (HOB) of the target, can be used to study the response of different geological media, and can be used to study the efficiency of coupling to the ground as a function of source energy. The EPEC experiment relies on the principal of hydrodynamic scaling[3] to study the strength of shocks and the velocities of shock propagation that are the same as would be achieved with high-energy sources in full-scale field tests, however, the EPEC phenomena take place over spatial and temporal scales that are orders of magnitude smaller than the full scales.

The EPEC experiment is driven by a low-mass ($\lesssim 1$ mg) target that is turned into a high-temperature plasma by 10 kJ of laser energy on time scales of a few nanoseconds; the energy per unit mass and energy per unit volume in the EPEC target are equal in a hydro-dynamic sense to those in a low-yield nuclear weapon or a large high-explosive charge. However, like the much smaller size of a low-yield nuclear device compared to an equal yield of chemical high explosive, the EPEC source is very small and allows us to study the coupling and partitioning of the source output at HOBs very near to the surface in a way that can not be done with high explosive, for which the size of a large-energy charge is greater than the heights of burst that may be of interest to study.[4,5]

In what follows below, we report on the blast and shock measurements made for three NIF shots that used a well characterized medium for a ground surrogate (namely BK-7 glass) and a custom atmosphere (discussed further below) to simulate in a scaled sense (§ I A) the full-scale field phenomena. We know of one previous study that used a laser to generate blast waves in a test atmosphere[6]. The work of Grun *et al.* used 100 - 150 J of infrared laser light to create blast-wave phenomena in a low-pressure ($\approx$5 Torr) atmosphere. Our shots spanned HOBs ranging from an infinite height of burst (that is, we removed the ground surrogate), 10 mm above the ground surface and 1 mm above the ground surface. The data we measured conform well to expected pressure and arrival time scalings from the literature[7,8]. It is our hope in the future to be able to use this platform to study with finer resolution the coupling effects of scaled nuclear-energy-density events for HOBs near the surface of the ground surrogate, as well as to study both shallow and deep depths of burial (DOBs). We believe that we can use the ground-surrogate medium to look at the effects of fault planes, cavities and inclusions (of, say, sand or water) on the propagation of near-source stress waves in geologic materials. This paper reports on the demonstration of the EPEC concept and its delivery of high-quality data from three NIF shots.

A. SCALING RELATIONSHIPS

The response of the test atmosphere and ground medium of the EPEC system has been modeled with the hydrodynamic code GEODYN[9–11]. The code was developed at LLNL and incorporates physical models to fully

describe a broad range of phenomena including shock and thermodynamic behavior. It is an Eulerian code with adaptive mesh refinement (AMR)[11]. In an Eulerian code, the mesh or background is stationary and the material is allowed to move though stationary cells. The adaptive mesh means that the code has the ability to vary the level of detail of the background.

Limiting ourselves to the case of a compressible hydrodynamic fluid (i.e., without the terms in the Cauchy stress tensor specific to solid bodies), the Euler equations assume the familiar form:

$$\frac{\delta \rho}{\delta t} + \vec{\nabla} \cdot (\rho \vec{v}) = 0 \tag{1}$$

$$\frac{\delta}{\delta t} (\rho \vec{v}) + \vec{\nabla} \cdot \left(\rho \vec{v} \otimes \vec{v} + \vec{\nabla} P \right) = 0 \tag{2}$$

$$\frac{\delta}{\delta t} (E) + \nabla \cdot (\vec{v}(E + P)) = 0 \tag{3}$$

where ρ is the density, $\vec{v}$ is the velocity vector, $\vec{v} = (v_x, v_y, v_z)$, P is the thermal pressure and $E = \rho \varepsilon + \frac{1}{2} \rho (\vec{v} \cdot \vec{v})$ is the total energy per unit volume, with ε being the internal energy per unit mass for the fluid. Equations 1, 2 and 3 remain invariant under the transformation (bearing subscript 1):

$$\begin{array}{ccc} \vec{r} = a\vec{r_1} & t = bt_1 & \rho = c\rho_1 \\ P = \left(\frac{a}{b}\right)^2 P_1 & \varepsilon = \left(\frac{1}{c}\right) \left(\frac{a}{b}\right)^2 \varepsilon_1 \end{array} \tag{4}$$

where a, b, and c are arbitrary positive numbers. There is a direct correspondence between any two systems satisfying equation 4. Noting that the pressure in a system is defined as the energy per unit volume in the system, we can relate the yield of the blast to the pressure at a point by:

$$\begin{aligned} W &= \int dV \left(\rho \varepsilon + \frac{1}{2} \rho (\vec{v} \cdot \vec{v}) \right) = \int dV P \\ &= \int (a^3) dV_1 \left[c \left(\frac{a}{b}\right)^2 P_1 \right] = \frac{a^5}{b^2} c W_1 \end{aligned} \tag{5}$$

where W represents the total energy in the system. For an above-ground detonation case, we can assume a constant density in the system at the two locations, i.e., $c=1$ in equation 4. Thus, for two systems with different total energies, when spatial and temporal dimensions scale by the same factor (i.e., $a=b$), we find the scale factor a is

$$a = (W/W_1)^{\frac{1}{3}}. \tag{6}$$

Thus, for the EPEC system driven by 10 kJ of energy, the scale factor for spatial and temporal parameters, when referenced to a 2.5 KT = 10^{13} J system, the scale factor is $a = 1000$. This factor (taking m to mm and msec to μsec) is very amenable to laboratory experiments.
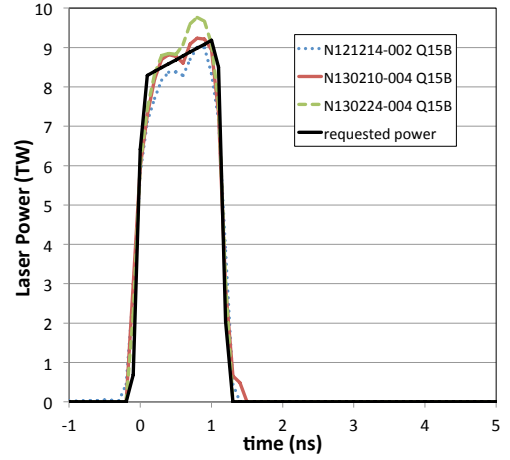

FIG. 1. (color online) NIF laser pulses from the 2013 Data Campaign shots.

II. THE NIF LASER

The NIF[1,2] is a 192-beam laser system now operating at the Lawrence Livermore National Laboratory (LLNL). The facility is capable of delivering up to 1.8 MJ of ultraviolet (351 nm) laser energy to mm-scale targets at the center of a 10 m diameter target chamber[12]. For the EPEC experiments described here, we used 10 kJ of laser light from 4 of NIF's 192 beams (one quad out of an available 48) to drive blast and shock phenomena in our experiment. The laser power was delivered to the EPEC target in an approximately flat-top pulse that was $\approx$ 1 ns wide; a collection of the delivered EPEC laser pulses is shown in Fig. 1, which gives one a sense of the reproducibility of the NIF laser.

We performed four shots to characterize EPEC target performance (see § III A 2) and four shots to get the ground shock and air-blast data for our target at different heights of burst above our ground-simulation surface. For the shots in our Data Campaign, we fired one shot to characterize the electromagnetic interference and other noise sources in the facility, and three fully instrumented EPEC shots at increasingly smaller heights of burst (see Sec. IV).

III. THE EPEC SYSTEM

In our Data Campaign, we made proof-of-principle measurements showing that blast effects, which are driven by a laser can be measured in a controlled, macroscopic, pressurized environment. We have measured the ground shock and dynamic atmospheric overpressure in our EPEC test assembly. We have also measured the optical power emitted by the x-ray deposition from our laser target in the test atmosphere. These proof-of-principle measurements are made for a pair of scaled heights of burst above a ground surrogate material.
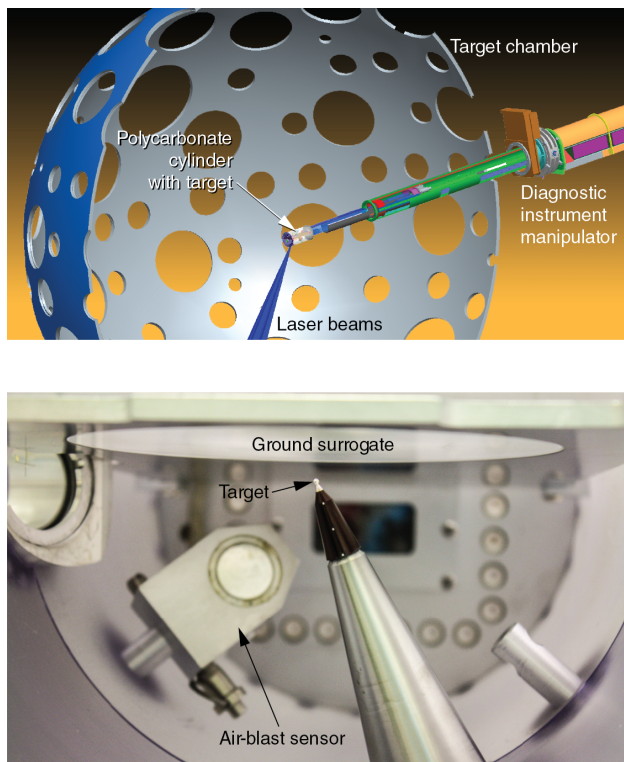
FIG. 2. (color online) (top) In the energy-partitioning, energy-coupling (EPEC) experiments at the National Ignition Facility (NIF), a diagnostic instrument manipulator inserts a pressure cylinder into NIFs 10-meter-diameter target chamber. (bottom) The photo shows the interior of the cylinder with a target, air-blast sensor, and ground surrogate installed.

The EPEC experiment is designed to be fielded in a diagnostic instrument manipulator (DIM)[13,14] at the NIF; the EPEC experiment is instrumented with pressure gauges at two stand-off distances (SODs) in the test atmosphere and two pressure gauges and one stress gauge at three depths in the ground medium. We report the details of the EPEC design in what follows. However, for a sense of scale and overall concept, we show the EPEC experiment in the 10 m diamenter NIF target chamber in Fig. 2, as well as an image of the interior of the EPEC system. Figure 3 shows the EPEC system being loaded into the NIF DIM; diagnostic technicians in the photo give a sense of scale. It should be noted that the diameter of the cylindrical EPEC chamber is at the absolute maximum allowable size to fit through the gate valve that isolates the NIF DIM from the NIF target chamber.

A. EPEC TARGETS AND ENERGETICS

The first phase of developing the EPEC experimental platform was to develop the energy source that would drive the blast and shock phenomena to be studied. For this, we developed a thin-walled spherical cavity (called a halfraum) that would convert the laser energy from UV
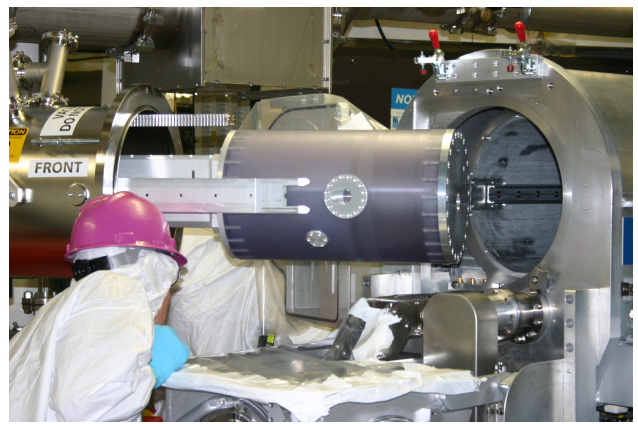

FIG. 3. (color online) NIF personnel prepare for the first EPEC data shot, which took place on December 14, 2012. Shown in the picture is the EPEC cylinder and air box assembly being loaded into the rear of a NIF DIM.

laser light into x rays and blast energy. The criteria driving the development of the targets were that the targets be strong enough to support vacuum on the interior, ie. the interior of the cavity shared the NIF target-chamber vacuum in order to allow the laser beams to propagate into the halfraum, and simultaneously, that the walls of the target be thin enough to allow a large fraction of the x rays generated in the halfraum to burn though the material and emerge into the test atmospheres. A short presentation of details about the actual fabrication of the targets are given in § III A 1, which is taken from Giraldez et al.[15].

It was critical to understand both the laser coupling to the target (not 100% of laser light is absorbed by targets in high-energy-density plasma experiments) as well as the x-ray performance of the target. Once the halfraum target that is the energy source for these experiments is embedded in the full EPEC system, we would be unable to use any of the NIF facility x-ray diagnostics or laser-backscatter optical diagnostics to make source-performance measurements. Thus, before performing any full-system blast and shock experiments, we performed a series of halfraum-only target shots to make the optical and x-ray measurements that were necessary to design the full system. A short presentation of details about the energetics measurements for the EPEC halfraums, our Energetics Campaign, are given in § III A 2, which is taken from May et al.[16].

1. DEVELOPMENT OF EPEC TARGETS

Details of the EPEC target fabrication performed at General Atomics (GA), and the target metrology performed at GA and LLNL, have been published in a peer-reviewed paper[15]. The EPEC target is a silver spherical halfraum 2 mm in diameter with a ≈ 7 μm-thick wall. The laser entrance hole (LEH) is ≈ 800 μm in diameter
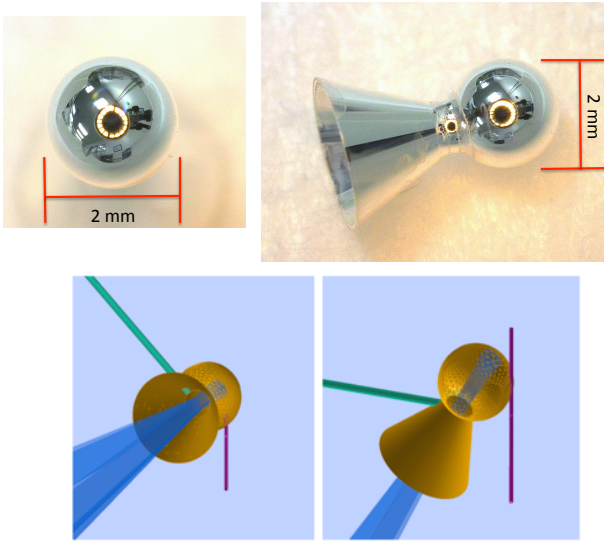
FIG. 4. (color online) (top) Top and side view of an EPEC halfraum target. (bottom) Orientation of EPEC target and laser beams with respect to two primary x-ray yield diagnostics.

and there is a conical skirt around the LEH. The conical section of thickness ≈ 100 μm is for structural support and to maintain vacuum during the experiment. This silver-based target is unique, to our knowledge no such target had been fabricated previously. A typical target is shown in Fig. 4.

The hollow silver spherical halfraum was fabricated by electroplating silver onto a spherical mandrel. An appropriate mandrel was needed, and the selection of mandrels was limited to metals that dissolve in strong bases or plastics that dissolve in organic solvents. Aluminum was first chosen since it dissolves in sodium hydroxide and it is also easily machined. However, it was observed that dissolution and removal of all of the aluminum was challenging, and sometimes small amounts of residue remained in the target. We moved towards using an acrylic based mandrel where residue is not an issue due to the complete dissolvability of the acrylic in solvents such as acetone. The challenge with acrylic was machining but this challenge was overcome and targets were successfully fabricated and fielded. All targets used for the Data Campaign were fabricated using acrylic mandrels.

The wall thickness of the silver sphere on the EPEC target was determined by analysis of x-ray images taken by a Xradia$^{\mathrm{TM}}$ system, a MicroXCT-200 x-ray microscope. This technique has been used in other x-ray dimensional measurements on shells.[17] To ensure that the Xradia would provide accurate wall thickness, the measurements were benchmarked by destructive characterization employing Focused Ion beam (FIB) cross-sections and scanning electron microscopy (SEM) analysis. The Xradia-derived thickness measurements matched the SEM results to within 1 to 2 μm.

2. ENERGETICS DATA

Details on the x-ray production from our EPEC targets, as well as an analysis of the budget of laser energy reflected, converted to x rays, and available for generating blast waves is given in May *et al.*[16]. A few observations and conclusions from that work follow. The time evolution of the x-ray spectral emission was measured by using the NIF Dante spectrometers[18,19]. The radiation from each target is recorded by using 18 separately filtered channels that cover discrete broad x-ray spectral bands between 50 eV to 10 keV with temporal resolutions of ≈ 150 ps. Two Dante spectrometers, 1 and 2, were available on the NIF for these experiments. Each had a different view of the target to help determine the energetics and laser coupling.

The x-ray flux that is created in the silver EPEC halfraum when driven by ≈ 10 kJ of laser energy is discussed in May *et al.*[16]. The interior radiation flux is nearly independent of the halfraum wall thickness for the three thickness shot: ≈ 8, 12 and 16 μm thick walls. Fig. 5 shows the x-ray flux that burns through the halfraum wall. The burn-through flux is measured with the Dante-2 detector, whose line of sight is shown on the left in Fig. 4. In the case of the burn-through flux, the wall thickness significantly affects how much radiation emerges from the halfraum wall. The radiation that comes through the halfraum wall is deposited in the EPEC test atmosphere and creates a "fireball" that expands and cools by emitting thermal radiation in the optical waveband. It is estimated[16] that approximately 7% of the incident laser energy is lost from the EPEC halfraum from the direct x-ray flux emitted from the laser entrance hole. In addition, it is estimated that $\approx 20\%$ of the incident laser energy is reprocessed by the thinnest-walled targets (the same targets we used in the Data Campaign) as x rays that interact directly with the EPEC atmosphere.

In all laser experiments, a portion of the incident laser light is reflected or backscattered from the target. These reflections are a result of resonant interactions of the laser electric field with plasma instabilities[20,21] and are mainly scattering from ion-acoustic waves (stimulated Brillouin scattering (SBS)) and from plasma-electron waves (stimulated Raman scattering (SRS)) in the plasma created inside the target. This backscattered laser light can be non-trivial and needs to be quantified for these halfraum targets. On a small number of NIF quads, the backscattered light is measured with the the Full Aperture Backscatter System (FABS)[22] and Near Backscatter Imaging (NBI) system[23]. The FABS system records the light backscattered from the target that is directed into each of the four incident drive beams. Since the scattering is a complex process, a good fraction of the light is scattered outside of the incident beam paths and is recorded by the NBI system. The scattered light is incident on special NBI scatter plates mounted to the NIF target chamber wall surrounding but not blocking the laser beam paths. The
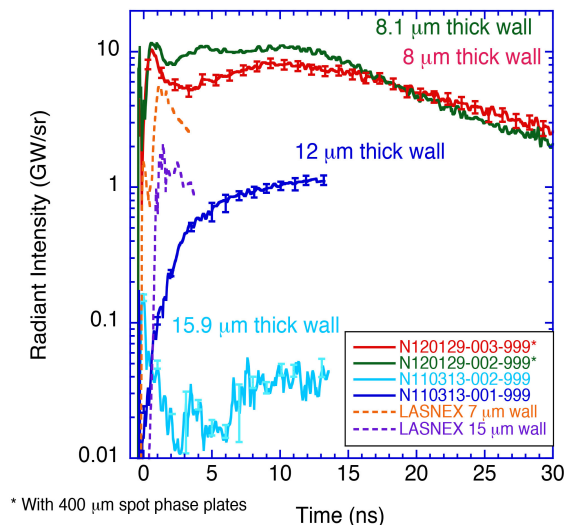
FIG. 5. (color online) The radiant intensity versus time for Dante-2 measurements from four spherical silver targets (previously published in May *et al.*[16]).

reflected laser light hits the scatter plates and is reflected into a set of gated imaging cameras. For the EPEC targets, approximately 7% of the laser energy is lost via backscatter in the case of defocused laser beams incident on the target, and only 1–2% when the beams' intensity profiles are smoothed with continuous phase plates (CPPs)[24]. As a result, CPP-smoothed laser profiles were used for all the Data Campaign experiments. Thus, for the case of smoothed beams on an EPEC target, we find that approximately 92% of the laser energy couples to the target (7% losses from x rays lost through the LEH, 1% loss from backscatter and other mechanisms), and, in the case of the thin-walled targets, 20% of the laser energy is converted into x rays that interact directly with the EPEC atmosphere.

B. EPEC VESSEL AND AIR BOX

Exhaustive analysis of the mechanical design and safety margins of the EPEC system have been published in a NIF Mechanical Engineering Safety Note[25]; here, we simply describe some of the parameters of the EPEC design.

In our Data Campaign the conical skirt of the target (see Fig. 4) is placed on the end of a stainless steel cone. The cone is the interface for the EPEC target and the NIF target-chamber vacuum, which is typically on order of 10^{-3} mTorr. The cone is part of an airtight vessel pressurized to one atmosphere in which the EPEC experiments will take place. The pressurized EPEC system is inserted into the NIF chamber before a shot through one of the facility's DIMs, and withdrawn afterwards. The vessel contains the one atmosphere of pressure in

the vacuum of the NIF target chamber until the target is destroyed, at which point the gases vent into the NIF target chamber. The target on the tip of the cone is suspended at various heights above our ground simulant (lower panel Fig. 2), which in this case is a 160 mm diameter block of BK7 (borosilicate) glass. The system is shown schematically in the 10 m diameter NIF target chamber in Fig. 2, along with a single quad of NIF beams (blue beams from the bottom of the figure) entering the cone that positions the target above the glass surface.

The integrated EPEC diagnostic system for the Data Campaign consists of two major components: a 158.75 mm square, 1422.4 mm long aluminum vacuum enclosure called an air box (with walls 12.7 mm thick), and a 297 mm outer diameter, 513 mm length polycarbonate cylinder. The assembly is shown being loaded into the NIF DIM in Fig. 3. Mounting rails on the side of the air box serve as the interface between the diagnostic assembly and the DIM cart/boat assembly. The mounting rails use tooling balls to align to a registered location in the DIM cart/boat assembly, which can be inserted by the DIM positioning system to a precise location in the NIF chamber. For the full EPEC assembly, the Opposed Port Alignment System (OPAS)[26] allows the diagnostic package to be positioned inside the NIF chamber to a tolerance of ± 100 μm with respect to target chamber center. The EPEC system is aligned by using a set of fiducial monuments that are visible in the lower panel of Fig. 2 on the black tip on the steel cone that supports the halfraum target. The fiducial positions are metrologized using the same optical technique used in the Energetics Campaign target metrology.

The walls of the polycarbonate cylinder shown in Fig. 3 are 25.4 mm thick. During the experiment the cylinder will be filled with a gas mixture (discussed below) at 1 atm pressure, and will see a very significant pressure spike up to 3000 psi for approximately a microsecond. To maintain the integrity of the cylinder during a shot sequence, the cylinder has 25.4 mm thick aluminum end plates that are each held on with 24 3/8-16, grade 9, socket head cap screws. The end and side alignment viewports were initially made of 12.7 mm thick, 50.8 mm diameter polycarbonate, and are each held in place with 16 5/16-18, grade 9, socket head cap screws. It was found during pre-shot testing that the polycarbonate had surface features that made accurate viewing of the target impossible for alignment, so they were replaced with fused silica. The target cone is made of 316 stainless steel. It is conical with an 8.5 degree taper over approximately 520.7 mm. It has a wall thickness of 3.175 mm. It is also held onto the cylinder with 16 5/16-18, grade 9, socket head cap screws. The cylinder, fully instrumented will weigh approximately 71 pounds. The full diagnostic, when mounted on the air box, will weigh slightly less than 240 pounds.
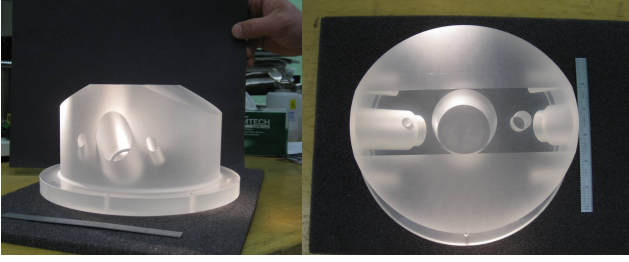
FIG. 6. (color online) The EPEC BK7 glass ground simulant (left) side view and (right) top view. One can see in the image a 6" ruler indicating the block's diameter. One can also see in the top view the three channels machined into the glass for the three ground shock-sensors.

C. ATMOSPHERE AND GEOLOGICAL MEDIUM

As discussed above, our system is a hydrodynamically scaled analog for blast and shock waves to propagate in an atmosphere and a geological medium. However, as also described above, much of the yield from our target interacts with the test atmosphere through the deposition of x rays, which don't obey hydrodynamic scaling. Thus, we designed an EPEC atmosphere[27] that attempted to increase the cross section for absorption of x rays by $\approx 1000\times$. This was accomplished by adding nobel gases to the atmosphere until the design simulations suggested that the deposition region around the EPEC halfraum would have a radius $\lesssim 1$ cm. The final composition of the EPEC atmosphere was 44% N_2, 21% O_2, 20% Ar, 10% Kr, and 5% Xe. It should be noted that the density of the EPEC atmosphere was 1.53×10^{-3} g/cm^3, while the density of sea-level air is 9.6×10^{-4} g/cm^3. In the final atmosphere, all x-ray energy from the halfraum target was deposited at a radius of 1 cm or less from the surface of the halfraum, thus producing a x-ray fireball with a scaled radius of <10 m (using the scale factor of 1000 discussed above).

A glass block was used as a surrogate material for earth. It was made from a single billet of Ohara S-BSL7 material (commonly referred to as BK-7 glass) by Schott$^{\text{TM}}$ Glass and machined into our specified shape by the Insaco Corporation. A photograph of the block in its final configuration is shown in Fig. 6. The glass block in the EPEC assembly housed two pressure sensors and a single quartz stress sensor. The bottom surface of the block was angled to allow it to fit into the cylindrical chamber that housed the EPEC system. The outer ring of the upper surface of the glass block (shown upside down in the left image of Fig. 6) is 200 mm in diameter, and was used to mate the Earth surrogate to an aluminum shelf in the EPEC cylinder (necessary to let the blast waves in the atmosphere travel beyond the edge of the block's surface). Also visible in the left picture is one of the bores that housed one of the PVDF-based pressure gauges that were installed in the glass block. The BK-7 was an acceptable material for these experiments because
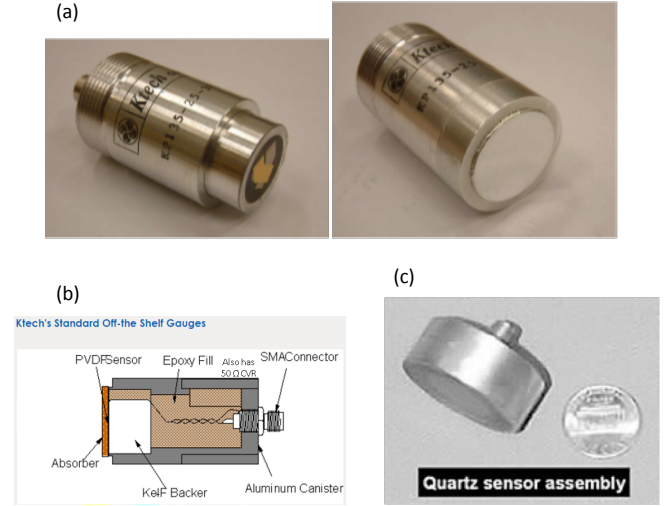

FIG. 7. (color online) (a) Ktech PVDF pressure sensor, model KP-135-25. These images show the sensor (left) before and (right) after the addition of the aluminized Teflon shield. (b) Cross-section of Ktech basic PVDF shock gauge. (c) Ktech quartz shock gauge, shown with a penny for scale.

its properties are well known and could be included in our simulations with high confidence.

D. SENSOR CALIBRATIONS

The EPEC system had seven high-bandwidth sensors to measure blast and shock in the air and ground surrogates and to measure optical radiation from the x-ray deposition in the EPEC atmosphere. There are also several low-bandwidth channels available in the NIF DIM that were used to monitor pressure in the EPEC cylinder and in the EPEC air box during shot cycles. The air blast and ground-shock sensors are described below. We will not discuss the optical power diagnostic system, built on two filtered photomultiplier tubes (PMTs), further in this work.

The sensors that were used to measure the ground shock and the dynamic overpressure in the EPEC atmosphere were provided by KTech Corporation (now part of Raytheon). Two types of pressure sensors were used in the EPEC Data Campaign experiments. One was a Ktech PVDF (polyvinylidene fluoride) shock gauge[28]. The thin film PVDF sensing area is 5 mm $\times$ 5 mm in size as shown in the left image at the top of Fig. 7. The sensor is protected by three layers of Teflon bonded in place; 0.0005 inch Teflon, 0.002 inch aluminized Teflon (aluminum side out) and a 0.001 inch FEP Teflon (not shown in the figure). The aluminized layer is bonded to the aluminum sleeve with conductive silver epoxy. A cutaway schematic view of the gauge is shown in the lower part of Fig. 7. The other type of gauge used was a Ktech quartz shock gauge[29] (lower right in Fig. 7). The quartz

shock gauge has the advantage of outputting voltage that is directly proportional to the measured stress, while the PVDF shock gauge outputs voltage that is the derivative of the measured pressure. One benefit of the PVDF shock gauge, however, is that it can measure useful data out to about 4 to 5 μs after the first edge of the incident wave arrives. The quartz gauge can measure useful data only out to about 1 μs after the incident waves arrival.

Calibration of the PVDF, both in and out of the glass block, and quartz shock gauges was accomplished using a shock tube at Ktech[30]. The calibration factor for the quartz gauges was determined to be 0.542 mV/bar for a 50 Ω impedance with an assumed accuracy of $\pm 5\%$. Accordingly, the expression for pressure retrieved (in bar) from the voltage at the terminals of the sensor into a 50 Ω load is

$$p(t) = v(t)/(0.542mV/bar). \tag{7}$$

Note that this assumes that cable compensation has already been performed on the recorded oscilloscope voltage to yield $v(t)$.

The calibration factor and pressure retrieval from the PVDF voltage is more complicated. The procedure for extracting pressure from the voltage at the terminals of the sensor into a 50 Ω load is:
1. Divide $v(t)$ (in Volts) by 25 Ω to get current in A. (25 Ω is the parallel combination of R and the 50 Ω load attached to the BNC connector.)
2. Integrate the current in time to get charge (C).
3. Divide by the sensor area (2.5×10^{-5} m^2) to get charge per unit area.
4. Divide by the gauge factor: 1.84×10^{-6} C / (m^2 bar).
Combining the steps above into one expression yields retrieved pressure in bar:

$$p(t) = 8.70 \times 10^8 \int_{-\infty}^{t} v(t')dt' \tag{8}$$

with $v(t)$ in volts. Note that this assumes that cable compensation has already been performed on the recorded oscilloscope voltage to yield $v(t)$. The assumed accuracy of the calibration factor, which is the scaling factor before the integral, is $\pm 5\%$.

Errors in the measurement system for the quartz shock sensor are easily understood since the quartz shock sensor outputs voltage that is directly proportional to the stress. For the quartz shock sensor, it can be assumed that the total error is the result of the error in the calibration factor; systematic errors, including the cable compensation errors; and a random component, mostly due to oscilloscope noise. The calibration error has already been given as $\pm 5\%$. The systematic errors from the cable compensation could be as great as $\pm 10\%$, based on an assumed approximately 2 dB uncertainty in cable attenuation. The random oscilloscope noise is variable depending on the full-scale vertical range, but is nominally 1 mV, which yields negligible error compared with the other terms. The total error for the quartz shock sensors

then is about $\pm 11\%$, assuming rms addition of the error terms. Straight addition of the error terms, however, yields a total error of $\pm 15\%$. The actual total error is most likely between those two values.

For the PVDF shock sensors, the total error is also the result of the error in the calibration factor; systematic errors, including the cable compensation errors; and a random component, mostly due to oscilloscope noise. The calibration error has already been given as $\pm 5\%$. The systematic errors from the cable compensation also could be as great as $\pm 10\%$, again, based on an assumed 2 dB uncertainty in cable attenuation. The cable compensation error would tend to enter into the error on the retrieved pressure in the same manner as in the case of the quartz shock sensor. The error due to the oscilloscope noise, however, is computed quite differently from the quartz shock sensor case. If it is assumed that the nominal oscilloscope noise is ± 1 mV, then the error to use for the retrieved pressure trace would be approximately ± 1.7 bar. Since the peak pressures that were measured were greater than 20 bar, the oscilloscope noise error term is less than $\pm 10\%$. Thus, the rms addition of error terms could be as high as about $\pm 15\%$ for the PVDF shock sensors. The straight addition of the error terms could be as high as about $\pm 25\%$.

As part of the preparatory activities for the EPEC data campaign, a "background" test shot was taken on Oct. 30, 2012 (NIF shot N121030-002-999). Unlike the EPEC data shots, the NIF laser was not fired into a silver halfraum target. Instead, for N121030-002-999, the EPEC system was installed in DIM 90-78 and inserted to a position 2 m from TCC. The EPEC cylinder was pressurized with room air that was held in the cylinder by a sapphire window over the end of the adaptor cap at the end of the EPEC alignment cone. All diagnostics in the EPEC system (two PMTs, two PVDF air-blast sensors) were activated and armed to record data. A gold disk target was positioned at TCC using the NIF target positioner. Hence, the disk target and the EPEC system were physically and electrically isolated from each other. Approximately 62 kJ of laser energy in six quads was delivered to the disk using the EPEC laser pulse shape (pulse shape EPEC_1.3ns_ramp2, see Fig. 1). The open disk target is known to produce the largest electromagnetic pulse of any target configuration commonly shot at NIF[31]. The point of this EMP test shot was to confirm that the EPEC sensors would function in the NIF EMI environment and to measure a background level to set a baseline for EPEC data-shot data acquisitions.

The PVDF pressure gauges recorded a time-varying baseline, see Fig. 8. The high-frequency signal shown in the lower images of Fig. 8 is not of concern since it occurs much earlier than the arrival of the EPEC signals of interest. The baseline drift that follows at later times (upper panels in Fig. 8) is indicative of the type of signal to be removed as part of the processing of the EPEC data signals. The shot was very valuable to subsequent EPEC data shots since it exercised the EPEC control
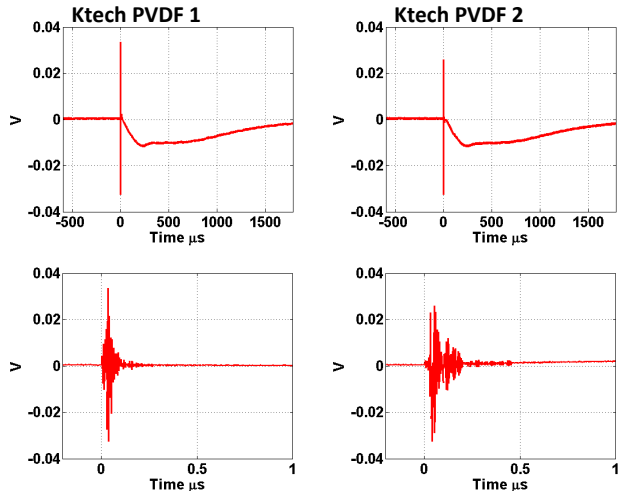
FIG. 8. (color online) EMP noise recorded on the two Ktech PVDF pressure gauges on NIF shot N121030-002-999.

system and the EPEC data-acquisition system through a real NIF shot cycle, and it confirmed that there were no excessively large leaks in our EMI shielding.

IV. MEASURED DATA

A. SHOT CONFIGURATIONS FOR DATA CAMPAIGN

The shot configuration for N121214-002-999 was for an infinite HOB. This configuration had two PVDF air blast sensors installed in the cylinder and two PMTs inside the air box. No glass block (earth surrogate) was installed (see top images in Fig. 9). The shot configuration for N130210-004-999 was a 10 mm HOB (bottom images in Fig. 9). This configuration had one air-blast sensor, the glass block with one PVDF and one quartz sensor embedded (two of the three sensors possible), and one PMT. We were only able to field four of the seven possible EPEC sensors due to the limitation of only four high-bandwidth channels in the DIM read-out capability. [Since the EPEC data shots were completed, the capability of one of NIF's equatorial DIMs has been expanded to support 16 high-bandwidth data channels.] The yellow object in Fig. 9 is the height-reference gauge block that was used to set the distance between the glass block and the EPEC target; it is used to set the height of the aluminum shelf before the glass block and shelf are installed as a unit. The shot configuration for N130224-004-999 was a 1 mm HOB with the same set of sensors operated as for N130210-004-999. Table I reports the measured initial fill pressures and measured atmospheric pressure at shot time for the three shots in the EPEC Data Campaign. The fill pressure at shot time and the actual gas density will be used in the scaling of EPEC data discussed below.

B. AIR BLAST

We begin with some definitions of common scientific terms that will keep the subsequent discussion clear:

Static pressure: The total pressure, including the ambient atmospheric pressure, also called absolute pressure, P_0

Overpressure: Equals static pressure minus ambient pressure, $P^o = P_0$ - P_{atm}.

Dynamic Pressure or Gust: The force per unit area caused by the mass motion of the gas. Usually defined $\frac{1}{2}\rho u^2$, where ρ is the air density and u is the air velocity in the arriving blast wave.

Stagnation Pressure: The pressure measured by a stagnation gauge. Equal to the sum of the dynamic pressure and the static pressure, $P_s = \frac{1}{2}\rho u^2 + P_0$.

Table II lists the measured values of data for the EPEC air-blast sensors on the three shots in the Data Campaign. The air-blast pressure sensors, described above, measure both the arrival time of the air-blast shock wave and, until reverberations of the gauge housing compromise the measurement, the stagnation pressure in front of the gauge. The measured shock-arrival times are accurate to $\pm 3\%$, the stagnation pressures are accurate to approximately $\pm 15\%$ (see Section III D). The PVDF air-blast sensors can record for approximately 3 μs before reverberations returning from the gauge housing overwhelm the signal. It is likely that the measurements were of very short duration compared to the full first-positive pressure wave, so an exponential fit to the decaying wave might be one way to extrapolate to an estimated longer pressure history (Kinney & Graham[7] describe such an approach). However, we have not done any extrapolation in the analysis that follows. Note, the lack of more than four high-bandwidth data channels in the NIF DIM meant that for the two shots that required ground-shock measurements, we were only able to run one air-blast gauge; the 15 cm gauge was chosen in both cases.

The gauges themselves are poorly impedance matched to the surrounding air, so the stagnation pressure in front of the gauge is converted to peak overpressure in the EPEC atmosphere in Table II. The peak air overpressure is found by comparing the atmospheric overpressure in the absence of a pressure gauge to the stagnation pressure in front of the gauge in the GEODYN simulations for each shot; this ratio is then applied to the measured stagnation-pressure data to give the overpressure in the test atmosphere.

Figure 10 shows the measured stagnation-pressure waveforms for the three data shots in this campaign. Note, there are two measurements for N121214 since it was an ideal air blast shot with no ground-shock sensors taking up read-out channels. One can see the peak pressures in the initial pulse followed by broader features at later times that we assign to reflected waves coming back off the gauge housing. The transit time for these reverberations is ≈ 3 μs, which is consistent with the radial-transit time for shocks to travel inward in the PVDF film
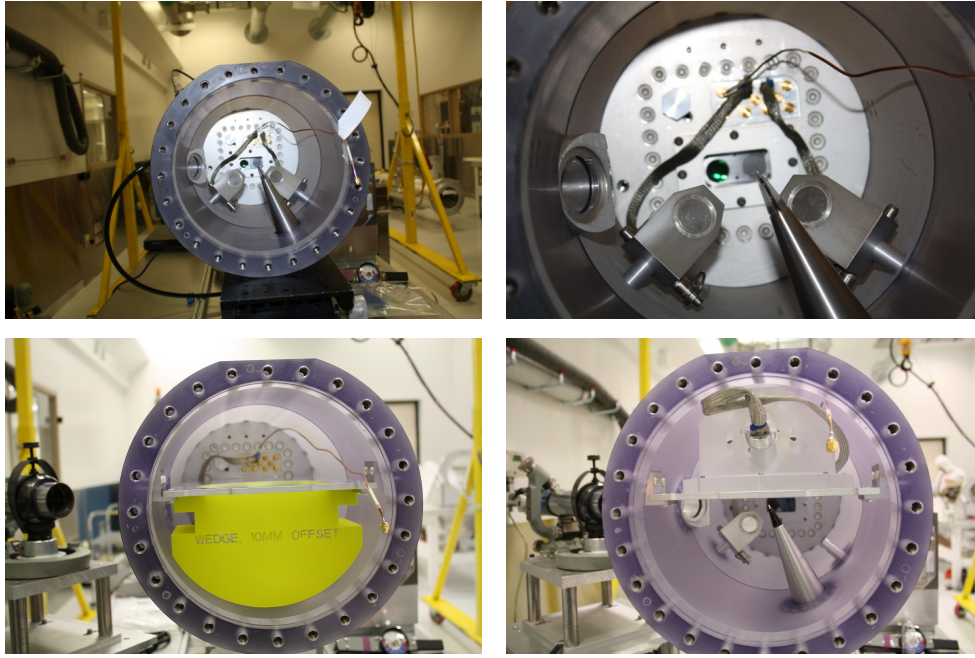
FIG. 9. (color online) (top) Left: View inside the EPEC cylinder before shot N121214 and right: Close-up of EPEC air-blast pressure sensors and PMT window at the back of the cylinder. (bottom) Left: View inside the EPEC cylinder as the gauge block is being used to place the EPEC ground plane before shot N130210 and right: EPEC air-blast pressure sensor, glass block and PMT window at the back of the cylinder ready for shot.

Shot number	E_{laser}	HOB	Initial fill pressure	Pressure at shot time	Sensor configuration
	(kJ)	(mm)	(bar)	(bar)	
N121214-002-999	10.2	∞	1.00	0.90	10 and 15 cm air-blast PVDF sensors
N130210-004-999	10.6	10	1.00	1.00	15 cm air-blast PVDF, 50 mm quartz, 50 mm PVDF ground sensors
N130224-004-999	10.8	1	1.00	0.88	15 cm air-blast PVDF, 50 mm quartz, 50 mm PVDF ground sensors

TABLE I. EPEC Data Campaign shot numbers, measured drive energy at the LEH, measured initial and shot-time fill pressure in the EPEC cylinder and sensor configurations.

in the gauges. In addition to the usual cable compensation and multiplication by a scaling factor, the PVDF data also require integration since the PVDF shock gauge outputs voltage that is the derivative of the measured pressure. The integration amplifies any low-frequency baseline offset in the PVDF data, so an approximation of the baseline offset (III D) must be subtracted to produce meaningful data. The waveforms in Fig. 10 are the baseline-subtracted, integrated and calibrated (according to Eq. 8) data that result.

Looking at the data for the 10 and 15 cm gauges in N121214, the shock arrival is at 56 and 120 μs, respectively, with peak pressure values of 115 and 28.7 bar. Note also that all three shots had a gauge at 150 mm from the EPEC target, which lets us compare the shock arrival times for the three cases of ideal air blast, 10 mm HOB and 1 mm HOB. As the EPEC target gets closer to the surface of the geological simulant (infinitely far, 10 mm and 1 mm), the shock arrival times get faster (120, 96

and 84 μs, respectively). This is likely due to a stronger reflection of the blast energy off the surface of the BK-7 glass block as the target gets closer to the block's surface. The reflected energy off the surface quickly overtakes the outgoing air-blast wave front and reinforces the pressure spike. The measured data in Fig. 10 have structure, both within the first peak that we define as the arrival of the (positive phase of the) air blast, and globally as reverberations compromise latter-time data. The peak pressures and delivered impulse (Table II) that we analyze below are taken from only the first pressure pulse. We could have fit an exponential curve to the decaying wave that is underneath the signal from the gauge reverberations and thus extrapolate to an estmiated longer first pressure pulse. However, we have not done any extrapolation and thus, derived blast-wave impulses may be as much as a factor of two low compared to the extrapolated cases.

Figure 10 also shows simulations for the stagnation-pressure waveforms for each shot. The simulations have

Shot	10 cm results					15 cm results				
	Time	Stagnation pressure	Over-pressure	Impulse	Simulated impulse	Time	Stagnation pressure	Over-pressure	Impulse	Simulated impulse
	(μs)	(bar)	(bar)	(bar-μs)	(bar-μs)	(μs)	(bar)	(bar)	(bar-μs)	(bar-μs)
N121214-002-999	56.2±1.7	115.0±17.3	22.3±3.3	187.5	201.7	120.0±3.6	28.7±4.3	7.85±1.2	58.09	80.9
N130210-004-999	–	–	–	–	–	96.7±2.9	68.6±10.3	15.8±2.4	91.76	199.7
N130224-004-999	–	–	–	–	–	84.1±2.5	–	–	–	94.4

TABLE II. EPEC air-blast results summary. Shown are NIF shot number, arrival time at the PVDF air-blast gauges, peak stagnation pressure measured at the gauge and the total impulse obtained by integrating the first positive phase of the overpressure waveform. Gauge data from N130224-004-999 were likely compromised due to damage to the detector from the earlier shots.
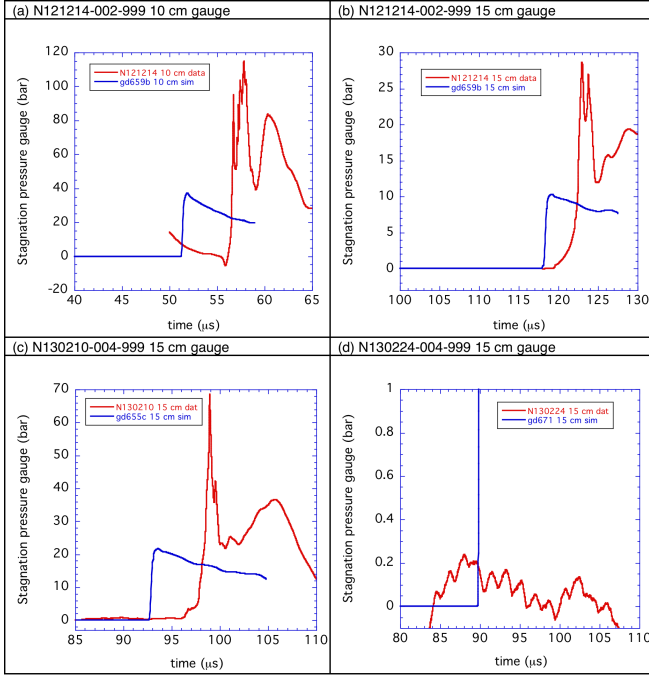

FIG. 10. (color online) Measured air-blast waveforms (red curves) from the EPEC Data Campaign for (a) shot N121214 at a 10 cm SOD from the EPEC target, (b) N121214 at 15 cm SOD, (c) N130210 at 15 cm SOD, (d) N130224 at 15 cm. Also shown in the figures are the results from post-shot simulations with GEODYN (blue curves). (Likely the gauge was damaged on the last shot.)

had the delivered NIF laser energy adjusted by the ≈0.71 kinetic-energy coupling factor that comes out of the Energetics Campaign data[16] (§ III A 2). From that starting point, fine adjustments were made to the energy source in the problem ($<$10% variation of the input energy) in order to optimize the predicted arrival time. The comparison with the data in Fig. 10 confirms the trends seen in the data: that the presence of the BK-7 ground plane accelerates the shock arrival time by ≈20% (compare the 15 cm gauge measurements for N121214 and N130210), and changing the HOB from 10 mm to 1 mm further accelerates the shock arrival time by ≈13%. In Fig. 10(a),

(b) and (c), the predicted peak stagnation pressures are between $2.5 - 3\times$ lower than the observed peak pressures in front of the gauge. This is not understood unless some overlooked effect is occurring (3-D effects not captured in 2-D simulations, radiation coupling or pre-heating of the gas not in our hydro.-only simulations, debris interacting with the sensor).

Table II compares the derived impulse from the measured stagnation-pressure data obtained by numerical integration and the impulse under the pressure wave in the corresponding simulation. The simulations have been integrated over the duration shown in Fig. 10. The time interval is $\Delta t \approx$7–9 μs for the simulation for N121214 (gd659b) and $\Delta t \approx$12 μs for the simulation for N130210 (gd655c). These intervals are larger than what is observed for the width of the first pressure pulse in the data: $\Delta t \approx$3 μs for the 10 cm gauge in N121214, and ≈4.5–6.3 μs for the 15 cm gauge in all three shots. The predicted duration of the pressure pulses are always wider than observed in the data, and thus, the impulse under measured and simulated pressure pulses agree somewhat better than do the peak pressures. Note, these are not the impulse numbers found by integrating the overpressure instead of the stagnation pressure that we measure in the experiment. From Table II, at the peak of the pressure pulse, the overpressure is typically $\sim \frac{1}{4}$ of the stagnation pressure. We would have to account for the velocity term in the dynamic pressure as a function of time [or total pressure] in order to deconvolve the overpressure waveform from the data in Fig. 10; this is beyond the scope of the analysis done so far.

1. AIR-BLAST DATA SCALING TRENDS

Much is known about the arrival times of air-blast shock waves from extensive work with chemical high explosives and the U.S. above-ground nuclear test program in the 1940s and 1950s (see chapter 3 of Glasstone[8], chapters 5 and 6 of Kinney & Graham[7]). The distance to which the blast-wave overpressure level will extend depends primarily on the energy yield of the explosion and on the height of burst. The maximum value, i.e., at the blast wave (or shock) front, is called the "peak overpres-

sure." Other characteristics of the blast wave, such as dynamic pressure, duration, and time of arrival also depend the energy yield of the explosion and on the height of burst. We define a "free air burst" as an explosion for which the presence of a reflecting surface, such as the ground, plays no role, and a "contact burst" as one for which given an ideal, perfectly reflecting surface, the shock wave characteristics, i.e., overpressure, dynamic pressure, etc., at the shock front would correspond to that for a "free air" burst that in the absence of a surface, has twice the apparent energy yield. This is important for comparing the first EPEC Data Campaign shot to the second and third. We compare the measured arrival times, peak pressures and total impulse in the first positive phase of the EPEC dynamic overpressure waveform to predicted values from the blast-wave formalism of Chapter 6 in Kinney & Graham[7]; the authors tabulate blast-wave quantities for both chemical and nuclear explosions in Table XI. By manipulating equation (6-2) in Kinney & Graham so that one can express shock arrival time as a function of the Mach number in the shocked gas, one finds the predicted shock peak-overpressure arrival time (equation 6-6) at a given range r from a blast;

$$t_a = \frac{1}{a_x} \int_{r_c}^{r} \left[\frac{1}{1 + \frac{(k+1)P^o}{2kP_atm}} \right]^{1/2} dr = \frac{1}{a_x} \int_{r_c}^{r} \left[\frac{1}{1 + \frac{6P^o}{7P_atm}} \right]^{1/2} dr \quad (9)$$

where r_c is the radius of the initial charge of HE or nuclear energy, a_x is the speed of sound in the undisturbed air, P^o is the peak overpressure, P_{atm} is the atmospheric pressure and k is the ratio of heat capacity at constant pressure over heat capacity at constant volume, c_p/c_v, which for an ideal gas can be approximated as k=1.4. Figure 11 shows the shock arrival time at a given distance for a 1 KT free air burst as calculated by Eq. 9 and tabulated in Table XI in Kinney & Graham.

In Glassstone's book[8], Kinney & Graham[7] and elsewhere authors plot blast-effects quantities against total explosion yield (ie., the sum of blast and radiation energy). In that spirit, we plot our scaled EPEC quantities against the total energy into the halfraum (that is 0.92 times the measured laser energy) based on the energetics measurements[16] in Sec. III A 2. As noted above, the post-shot simulations were run with energies approximately 0.71 times the laser energy, which allowed the simulations to agree with the measured air-blast arrival times at the EPEC gauges.

The EPEC air-blast sensors indicate that arrival times are on the order of 50 microseconds for the 10 cm gauge and on the order of 100 microseconds for the 15 cm gauge. The EPEC spatial and temporal values can be scaled to a 1 KT reference system according to

$$r_{scaled} = r_{EPEC} \left(\frac{4.18 \times 10^9}{E_{laser} \cdot \eta} \right)^{1/3} \left(\frac{P_{fill}}{P_{atm}} \cdot \frac{\rho_{fill}}{\rho_{air}} \right)^{1/3} \quad (10)$$
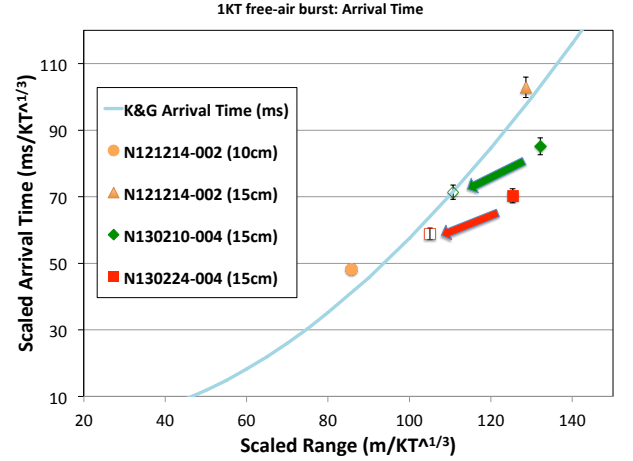

FIG. 11. (color online) EPEC air-blast sensor blast-wave-arrival times from Table 7.3 scaled to the full-scale dimensions for a 1 KT reference free-air burst. Also shown is the analytical expected shock arrival-time curve from Kinney and Graham[7]. The arrows linking filled to open symbols represents the correction factor for a contact burst.

and

$$t_{scaled} = t_{EPEC} \left(\frac{4.18 \times 10^9}{E_{laser} \cdot \eta} \right)^{1/3} \left(\frac{P_{fill}}{P_{atm}} \cdot \frac{\rho_{fill}}{\rho_{air}} \right)^{1/3} \left(\frac{T_{fill}}{T_0} \right)^{1/2} \quad (11)$$

where r_{EPEC} and t_{EPEC} are the physical air-blast sensor position and the measured air-shock arrival time, respectively, 4.18×10^9 is the energy in 1 KT in kJ, E_{laser} is the measured NIF energy, and η is the coupling factor from the EPEC Energetics Campaign. The pressure and temperature factors in equations 10 and 11 follow from equations 3.65.2 and 3.65.3 in Glasstone and account for the effect of altitude on blast phenomena when compared to an ideal air blast at sea level. In equations 10 and 11, P_{fill} is the measured in-vessel pressure at shot time (Table I) and P_{atm} is sea-level atmospheric pressure. The corrections are significant in field-scale problems at altitudes >5000 ft, however, since we did have pressure variation in the EPEC cylinder, we apply the correction to the scaled data in the figures that follow. Since the EPEC atmosphere was not chemically identical to air, we have modified the traditional pressure-scale-factor correction in equations 10 and 11 to account for the different densities of the EPEC fill gas, ρ_{fill}, and the density of air, ρ_{air}. The temperature term in eq. 11 arises because the speed of sound is proportional to the absolute temperature of a gas; we did not measure the temperature of the EPEC gas, and we assume that term is identically 1.

Plotted in Fig. 11 are the measured arrival-time data from the 10 cm EPEC air-blast gauge (N121214-002-999), and the 15 cm EPEC air-blast gauge (N121214-002-999, N130210-004-999 and N130224-004-999), scaled as described by equation 11. The measured arrival times are considered accurate to better than ±3%. The EPEC

data, when scaled in both time and space to a 1 KT reference yield match the expected curves to ≈5 - 10% for the measurements from N121414. This case was the "free air burst" case for EPEC without the ground plane present. The agreement is extraordinary given the unknown effect of the unique EPEC air chemistry.

Fig. 11 also has the scaled arrival times for the pressure signals from N130210-004-999 (filled diamonds) and N130224-004-999 (filled squares), which were a 10 mm and 1 mm HOB (≈7.5 and 0.75 m scaled HOB relative to a 1 KT blast), respectively. These are "contact bursts" rather than free-air bursts, which means that some (or all) of the blast energy is reflected from the ground surface and interacts with/reinforces the initial outgoing blast wave. The measured (scaled) points for N130210 and N130214 have arrival times earlier than the empirical free-air burst curves in Fig. 11. This is as expected since the reflected energy off the ground surface increases the apparent yield of the EPEC reference system, which, when scaled to a 1 KT free-air-burst arrival time, would arrive at a fixed position faster. If we multiply the E_{laser} measured source energy for N130210-004-999 and N130224-004-999 by a factor of 1.7, consistent with high pressure factors for a contact burst, we find that the measured and simulated points agree with the 1 KT free-air-burst curves to ≈5% (the open diamond and square in Fig. 11).

Kinney & Graham give an analytical expression (eq. 6-3) for the overpressure versus distance for a 1 KT explosion:

$$P^o/P_{atm} = 3.2{\times}10^6 r_s{}^{-3}\sqrt{1 + \left(\frac{r_s}{87}\right)^2}\left[1 + \frac{r_s}{800}\right] \quad (12)$$

where P^o/P_{atm} is the ratio of explosion overpressure to ambient atmospheric pressure and the term r_s is a "scaled range" like that in Eq. 10. This function has been normalized to both numerical calculations and experimental data and is thought to be accurate to ±10% for scaled distances < 300 m. Resulting data are tabulated in Table XI for (part A) 1 kg of chemical high explosive (HE) and (part B) on KT of nuclear yield. The EPEC gauge stagnation-pressure data have been measured in absolute units. These data are then converted to EPEC-system overpressure as described above for Table II (ie., by comparing the ratio from the simulations of stagnation pressure at the gauge face [in a simulation with the gauge in place] to the internal pressure at the same location [in a separate simulation without a gauge present]). We plot in Fig. 12 the EPEC in-air overpressure from the measured values at the scaled radial positions given by r_{scaled} in Eq. 10, and the expected free-air overpressure value for the 1 KT reference system[7] for both HE (red dashes) and nuclear (cyan) yields. The EPEC data have been scaled by

$$P^o_{scaled} = P^o_{EPEC}\cdot\left(\frac{P_{atm}}{P_{fill}}\cdot\frac{\rho_{air}}{\rho_{fill}}\right) \quad (13)$$

where P^o_{scaled} is the in-air overpressure at the gauge face

derived from the EPEC in-air data P^o_{EPEC} in Table II, scaled by the ratio of shot-time-measured EPEC fill pressure to sea-level pressure (eq. 3.65.1 of Glasstone[8]) and scaled by the ratio of the EPEC fill gas and air densities. The EPEC-measured data have ±25% error bars, the maximum value from § III D. The values of the EPEC air overpressures for shot N121214-002-999, our free-air burst, are ≈2× the empirical values for the nuclear curve; this is slightly surprising given that the scaled arrival times (Fig. 11) are quite close to the empirical trend. However, the scaled peak overpressure from the free-air-burst simulation (gd659) agrees very well with the peak in-air overpressure nuclear-yield curvie from Eq. 12. (The scaled radii for the NIF shots are different than the scaled radii for the corresponding simulations since the coupling factors, $\eta = 0.92$ and $\eta = 0.71$, respectively, are different.)

For shot N130210, our 10 mm HOB, the measured in-air peak overpressure at the 15 cm gauge is ≈4× the value expected from the nuclear-yield curve from Eq. 12. However, here we know reflections off the surface of the BK-7 glass block affect the shock strength. It is likely that the measured pressure for N130210 represents the superposition of a free air blast shock wave and the reflected shock wave; the curves from Kinney & Graham are for a free air-blast only. The discrepancy drops to ≈2× if we modify the actual drive of the shot, E_{laser}, by the contact burst enhancement factor of 1.7 (open green diamond in Fig. 12). As seen above, the measured data from N130224 are very weak, likely indicating either a gauge malfunction or nearly total coupling of the blast energy to the ground surrogate for this HOB, and are not plotted. It is interesting to note, but perhaps coincidental, that the scaled EPEC measurements lie along the empirical curve for 1 KT of HE yield. Also in Fig. 12 is a reproduction of the figure from Grun et al.[6] that shows their measured laser-created-shock peak pressures at appropriately scaled distances, which are much smaller than the EPEC scaled distances. In the case of the NRL data, the measured points conform well to the trend shown by the nuclear-scaled curve from Kinney and Graham. It is worth noting that the nuclear and HE curves from Kinney and Graham diverge sharply below ≈30 scaled meters, and differ by a factor of 10 for a scaled distance of 10 m/KT$^{1/3}$. The very high energy density of laser-created blast sources is an attractive way to study the dynamics of shockwaves at these very close distances to the blast. We note that the recent work of Ford et al.[5] has also studied the scaling of peak pressures with HOB for HE charges; their data for measured peak pressures from above-ground blasts start at a scaled distance of ≈3000 m/KT$^{1/3}$ (see their Figs. 14 and 15).

We have plotted the GEODYN values for the peak in-air overpressures from simulations gd659b (for N121214), gd655 (for N130210), and gd671 (for N130224) in Fig. 12, and we find, as we see in Fig. 10, the GEODYN-calculated peak pressures match the measured values to no better than a factor of three. This means that what-
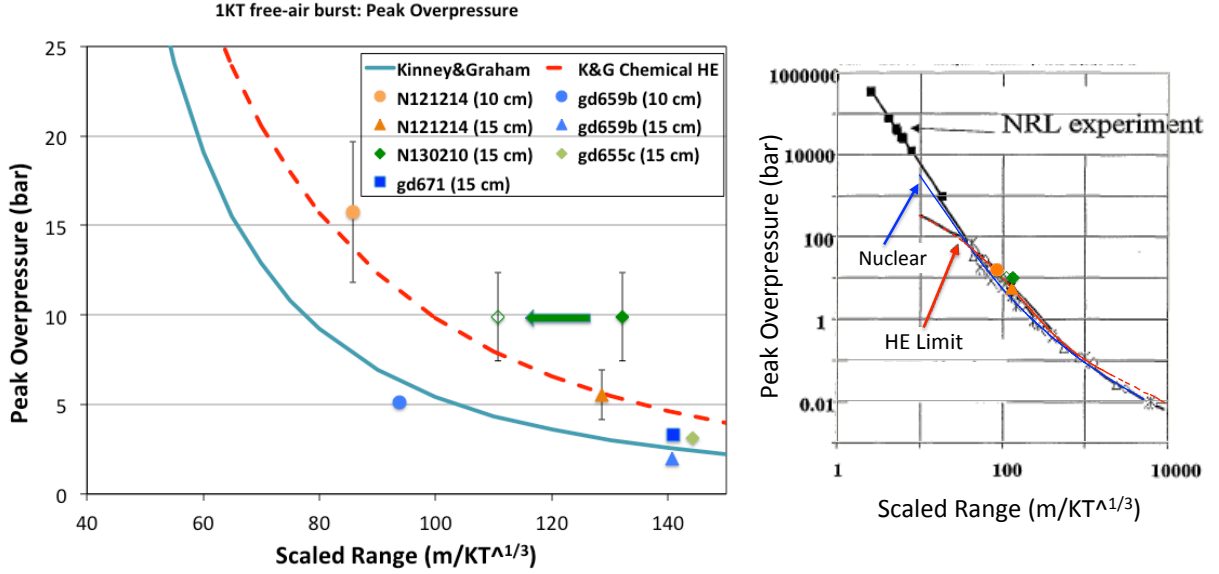
FIG. 12. (color online) (left) EPEC air-blast sensor peak overpressure values from Table II scaled to the full-scale dimensions for a 1 KT reference free air burst, and the expected peak air-blast dynamic overpressure values from Kinney and Graham[7] for 1 KT nuclear (cyan, solid) and chemical high explosive (HE) (red, dashed). The arrow linking the filled to open symbol represents the correction factor for a "contact burst". (right) Reproduction of figure 3 from Grun[6] with the older NRL data and the EPEC data on a logarithmic scale.

ever reason the code has for globally under-predicting the peak shock pressures (poor equation of state for our test atmosphere, poor model for the piezoelectric film in our pressure gauges) is consistent in the two post-shot simulations for measured data.

Although not a very likely confounding factor in the measurements of air blast, the simulations did show that the maximum angular distribution of debris from the target skirt and adapter tip is nearly perpendicular to the laser cone axis (±20 degrees or so). It is also possible for some of that debris to be traveling as fast as the average wave transmission speed over ranges of 15 cm. Thus, there is a finite possibility (probably low) that debris (or unusually high mass flux) occurs in the proximity of the air blast sensor (the timing of such is unknown, though). It is just a confounding factor that might be considered (and could also contribute to observed structure in the measured air-blast waves).

C. GROUND SHOCK

Table III summarizes the ground-shock sensor distances, measured arrival time, and the measured peak pressure or stress. The two sensors in the BK-7 ground simulant were a X-cut quartz gauge whose surface is at a DOB 5 cm directly below the blast point of the halfraum. We refer to this as 0° since it is directly below the target in the center of the glass block (see the large-diameter central bore in Fig. 6). The other gauge run on shots N130210 and N130224 was a PVDF pressure gauge the

center of whose face was at a DOB of 3.2 cm below the glass on a line of sight 50° with respect to the surface of the BK-7 glass block and the 0° line defined by the center of the quartz gauge. This means the path from the glass surface to the center of the gauge's face is 5 cm along the 50° vector from the glass directly under the burst point to the center of the gauge's face.

There are two numbers for arrival time in Table III for the quartz gauge on shot N130210-004-999, we hypothesize that is due to a shock wave off the glass that is initiated by x-ray blow-off that then propagates upwards towards the expanding halfraum debris, interacts with the debris/gas shock front and rebounds back towards the glass and then propagates in the glass ahead of the main shock wave from the arriving halfraum explosion. The ≈300 ns difference between the arrival of the reflected x-ray-induced shock wave and the main shock wave is very close to the value calculated in post-shot simulations (see discussion below regarding the simulations for N130210-004-999).

Figure 13 shows the measured stress (frames (a) and (c)) and pressure (frames (b) and (d)) waveforms (red curves) recorded by quartz and PVDF gauges, respectively, in the EPEC BK-7 glass block on shots N132010 (10 mm HOB) and N132024 (1 mm HOB). Also shown are simulated waveforms (blue curves) at detector locations in the block. The pulses measured in the geological surrogate are much narrower than the corresponding pulses in the air-blast sensors shown in Fig. 10. The PVDF-measured pressure pulses in our BK-7 block (frames (b) and (d)) are on the order $1 - 2$ μs wide, with

| Shot number | Energy | Quartz gauge, 5 cm, 0° | | PVDF gauge, 3.2 cm, 50° | |
| | | Arrival time | Peak stress | Arrival time | Peak pressure |
	(kJ)	(μs)	(bar)	(μs)	(bar)
N121214-002-999	10.2	–	–	–	–
N130210-004-999	10.6	8.24±0.25/8.53±0.26	2245.7±247.0	6.88±0.21	67.5±10.1
N130224-004-999	10.8	8.24±0.25	>10,900	6.42±0.19	52.8±7.9

TABLE III. EPEC ground shock results summary. Shown are NIF shot number, measured drive energy at the LEH, arrival time and peak stress at the X-cut quartz stress gauge (5 cm, 0 degree), and arrival time and peak pressure at the PVDF pressure gauge (5 cm, 50 degree).
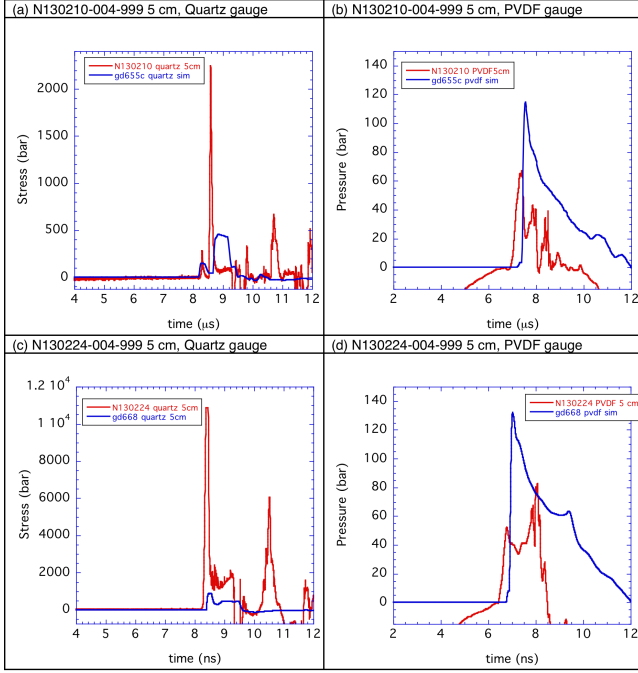

FIG. 13. (color online) Measured ground-shock waveforms (red curves) from the EPEC Data Campaign from shot N130210 for (a) quartz gauge stress measurements at a 5 cm DOB below the surface of the EPEC glass block, (b) PVDF gauge pressure measurements at a 3.2 cm DOB below the surface of the EPEC glass block, and from shot N130224 for (c) quartz gauge stress measurements at a 5 cm DOB below the surface of the EPEC glass block, and (d) PVDF gauge pressure measurements at a 3.2 cm DOB below the surface of the EPEC glass block. Also shown in the figures are the results from post-shot simulations with GEODYN (blue curves).)

a clear ramp from the initial arrival of the pressure pulse to its peak value. The ramp is due to the non-radial component of the pressure wave in the glass as strong surface waves are launched by the propagating strong shock in the air above the glass-block surface. The surface waves propagate down into the BK-7 block and sweep across the face of the PVDF pressure gauge. The simulations do not show the ramp in the pressure waveform because the gauge location in the simulation tracks the pressure at only a single mesh point and not across a finite surface.

The stress-sensor responses, frames (a) and (c) of Fig. 13, have even faster rises than the pressure waveforms; in this case the stress gauge is directly under the blast point and thus does not see the non-radial component of the pressure wave due to the surface waves described above. We note in the 10 mm HOB shot that there is a precursor seen in the stress-gauge data (and reported in Table III) that arrives ≈300 ns ahead of the main stress wave. The precursor is due to a shock wave launched very close to t=0 from an x-ray-created ablation response at the surface of the glass. This x-ray-created shock wave propagates into the glass giving rise to the observed initial peak, while blow-off material goes upward and interacts with the expanding cloud of halfraum-plasma debris. The waveform shown in Fig. 13(a) displays the initial shock from this x-ray-created pulse followed by the stress signature of the arrival of the main (much stronger) halfraum blast wave. Note that by the time these signals have arrived at the detector, they have propagated through 10 mm of our EPEC atmosphere and 50 mm of the BK-7 glass medium. The shocks propagate in the glass with a velocity ≈(50/7) mm/μs = 7.1 km/s, which is slightly more than the sound speed in the glass of 6 – 6.4 km/s.[32]

The GEODYN-simulated waveforms in Fig. 13 show excellent agreement for the arrival time of the shock waves at the locations of the stress and pressure gauges. However, as in the case of the air-blast results discussed in Section IV B, the peak values of stress and pressure differ from the measured data. For the PVDF pressure gauge in the BK-7 block, the predicted values are typically 2× higher than the measured values. For the case of the predicted peak stresses, the opposite is true and the measured values greatly exceed the results from the simulation. In the case of shot N130224-004-999, we measured almost no air-blast response, and as seen in Fig. 13(c), an extremely strong ground shock response. The simulation under-predicts the X-cut quartz stress gauge response by an order of magnitude. Circumstantially, this would suggest that shot N130224 was fully coupled to the ground surrogate medium. This may have been the case, rather than an air-blast gauge failure. We note the simulation for the PVDF pressure gauge in the glass block (frame (d)) is reasonably well matched to the peak-pressure data, pressure arrival time, etc. At the moment, the results from the 1 mm HOB shot N130224 are not fully understood.

Figure 14 shows images from a GEODYN pre-shot simulation of the EPEC 10 mm HOB shot N130210-004-999. The simulation was run with 9.4 kJ sourced into the blast phenomena and allowed to evolve. The simulation has the EPEC atmosphere, the energy pill that is the EPEC source at $r = z = 0$ mm (ie., the center of the problem's mesh) and the BK-7 glass block starting at $z = -11$ mm (the center of the halfraum is at $z = 0$, so the hafraum radius extends to $z = -1$ mm). The first frame is at t=163 ns, and we see that, initially, a small section of the glass is pre-heated by x-ray deposition. By this time there is a high temperature (20 eV or 220,000 K, red color) "fireball" of radius ≈ 10 mm with an ≈ 10 eV surface (bright green color), just barely reaching the surface of the glass block (right-hand side of the figure), and a larger (≈ 20 mm) preheated precursor expanding away from the fireball. The second frame, $t = 329$ ns, shows that by ~ 300 ns, the initial blast wave has reflected off the surface of the glass back towards the target (pressure evolution on the left-hand side of the center of the figure). The ≈ 10 eV surface of the fireball has expanded radially to ≈ 20 mm (right-hand side) and there is a knot of high pressure near where the tip of the EPEC cone used to be (left-hand side). Frame (c) shows that by ~ 400 ns, the reflected blast wave, which is moving radially outward, is interacting with and reflecting off the silver plasma; the shock from the initial contact propagates in the glass. The initially reflected blast wave is following the original outgoing blast wave in the air (ie., two thin red shells on the left-hand side of frame (c)). By ~ 650 ns (frame (d)), the main blast wave is now propagating in the glass; the initially reflected shock wave has caught up to the original outgoing blast wave along the ground surface and begins formation of a Mach stem (left-hand side of the image, near $r = -20$ mm). The high-temperature part of the fireball (right-hand side of the image) is being compressed and directed up and away from the surface of the glass. At the time of this image, one can clearly see high-temperature debris moving back up the EPEC laser cone at high velocity. Frame (e) shows the initial ground shock wave and the second, stronger ground shock wave are separated by ~ 500 ns. The strong blast wave traveling in the air over the surface of the glass has fully merged with the initial outgoing radial air-blast wave and launches stress waves into the glass. There is still a strong high-pressure feature at the Mach stem on the surface of the glass (leftmost feature in the image at $z = -11$ mm). Looking in the glass block ($z < -11$ mm) one can see the shape of the pressure pulse in the glass is much flatter than if it continued the spherical shape of the blast wave in the air. It is this distortion from spherical that introduces the finite time of the sweep across the oblique pressure sensor in Fig. 13(b) and (d). At ~ 2 μs, frame (f), the air blast and its interaction with the surface of the BK-7 block has formed a Mach stem, the surface waves and the shock wave from under the target have merged. The reflected wave from the surface has fully merged with the initial outgoing airblast (well above the ground surface).
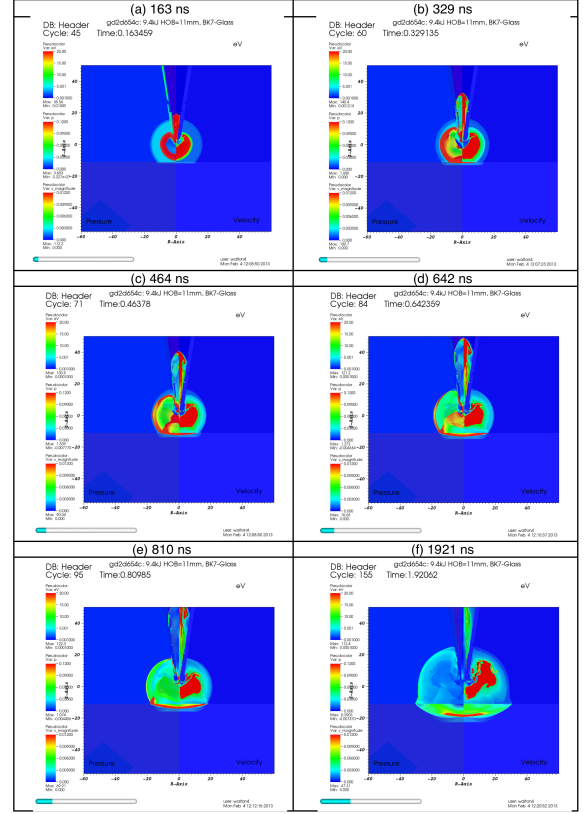

FIG. 14. (color online) Snapshots from the GEODYN simulation of the 10 mm EPEC HOB shot N130210-004-999. The left-hand side of each frame is a color-plot of the pressure in the system, the right-hand side displays the color map of the temperature (for $z > -11$ mm) and the velocity field of shock waves in the glass medium ($z < -11$ mm). The halfraum is placed at $r = z = 0$ mm and the block of glass starts at a height of $z = -11$ mm. The time in the simulation at which each image is capture is written above the image.

1. GROUND-SHOCK DATA ANALYSIS

Seismic measurements are classified into a heirarchy of increasing distances from the source of the disruption: near, far, regional, and teleseismic. Although for both of the EPEC experiments with the ground plane in place (N130210 and N130224) there was melting and/or cratering of the surface, the medium at the location of the shock measurements was in the elastic regime.

The seismic observables used for actual forensic analyses of blasts, tunnel collapses, etc. are displacement, velocity and acceleration. Seismometers, key diagnostic tools of seismic signatures, measure only displacement. Previous researchers[33,34] have noted that only displacement legitimately follows cube-root scaling analogous to the types presented for air-blast effects in Section IV B 1. Koper et al.[4] have concluded that the peak displacement

of the first seismic-signal arrival is the most robust estimator of the yield of the source of all the observables they studied. Ford *et al.*[5] have demonstrated a model where seismic displacement and atmospheric overpressure impulse together provide a good determination both yield and HOB/DOB for sources with unknown emplacement. Seismic signals are usually quantified as being in the far field, being outside of the elastic region, or in the near field, when the ground is still in the elastic regime. Our EPEC measurements are made in the very near field to the nuclear-energy-density source (a scaled depth of burial on the order of 38 m) and only measured the geological arrival time as well as the peak stress or peak pressure caused by the displacements traveling in our geological surrogate medium. We did not measure any of the displacements that are usually measured by seismometers. Thus, we do not present any of the scaling trends of the type we presented for air blasts in Section IV B 1.

The concept of equivalent yield, W_e, defined as the yield of a contained nuclear explosion that would produce the same motion and stress field as a near-surface burst of yield, W, was introduced by Cooper[35]. Coupling curves have been developed that provide an equivalent-yield-factor as a function of height of burst (HOB) or depth of burial (DOB), as a means of providing guidance for the effectiveness of near-surface nuclear explosions in generating ground-shock waves. The equivalent-yield-factor is simply the equivalent-yield divided by the total-yield. The coupling curves usually used for this purpose provide best-estimates for equivalent yield factors for peak accelerations, velocities and stresses in the range of about 1-kBar. They are based primarily on estimates of downward directed stress waves immediately below the explosion source.

Based on the coupling curves in customary references[8,36] for near-surface air bursts the nominal coupling factor varies from a value of 0.02 at 'contact' (HOB=zero) to a value of ~0.015 at a scaled height of 8 m/kT$^{1/3}$. This is a change of only 25% over a change in scaled HOB from zero to a height which would correspond to a height of ~11 mm above the surface in the EPEC configuration. In the two near-surface-burst EPEC experiments the peak stress measured at a depth of 50 mm below the glass surface was ~2.2 kBar for the HOB=10 mm (shot N130210 at a scaled HOB ~7.5 m/kT$^{1/3}$), and >10.9 kBar for the HOB=1 mm (shot N130224 at a scaled HOB ~0.75 m/kT$^{1/3}$), an increase of >5×. This is inconsistent with a change of only a few percent in effective yield factor that would be predicted for that same change in scaled height of burst using the conventional coupling curves for near-surface explosions[36]. We believe that this dramatic sensitivity in coupling with HOB for near-surface bursts in the EPEC tests is a result of the x-ray energy coupling into the glass (i.e., ground) surface in a manner that may not be very similar to the physics associated with near-surface nuclear explosions. The conventional coupling curves are based on simulations most probably using hydro

only, with no radiation coupling to the ground, and thus, may not accurately account for the effects of x-ray deposition from near-surface nuclear explosions. The EPEC hohlraum design was specifically selected to simulate the hot plasma of a typical fireball that would result from a nuclear explosion. X-ray energy from such ionized material is transported to the surrounding atmosphere and the nearby ground surface, thereby greatly increasing the effective yield coupling to the ground over what would occur without any radiation transport. It should be noted that the preshot and postshot GEODYN hydrocode simulations of the EPEC experiments were hydro-only simulations with some, arbitrary, manual redistribution of 20% of the total energy to crudely approximate the effects of radiation transport. This was a well motivated first-order approximation of relevant physics based on our Energetics Campaign results and off-line simulations of radiation deposition in the EPEC atmosphere[27]. However, those hydrocode simulations were of insufficient fidelity, with respect to radiation transport, to provide accurate predictions of the x-ray coupling into the glass (i.e., ground) surface. A more sophisticated treatment is called for in simulations (i.e., including rad-hydro coupling) for any follow-on EPEC-like tests.

V. CONCLUSION

We conclude this report with the statement that the EPEC project met its goal of demonstrating that experiments that replicate the phenomena found in above-ground nuclear tests (AGTs) can be performed at the NIF. Specifically, we have demonstrated that we can make air-blast shock arrival and peak-pressure measurements that scale approximately to the values expected from AGTs with a 1 KT yield. We have demonstrated that we can measure large stresses and pressures in the ground surrogate used in the EPEC tests. These stress responses can be simulated with state-of-the-art geophysical computer codes. However, our hydro-only simulations, with an arbitrary (assumed) radiation energy deposition on the glass surface, did not match the measured pressures immediately below the shot point. The simulation pressures at the location of the oblique sensor (i.e., at a horizontal range of ~3.83 cm) were within a factor of two of the measured pressures (probably indicating less sensitivity to radiated energy deposited on the glass surface at this horizontal range). We have not been able to directly correlate the near-field-measured EPEC ground-shock phenomena with seismic displacements from near-surface nuclear or HE tests. In future experiments, we will explore different ground-shock detectors and embed those detectors in real geological materials (limestone, sandstone, granite, etc.). We were able to do three shots during the project that represented a free air burst (N121214), a contact burst with a scaled HOB of ≈7.5 m/KT$^{1/3}$ (N130210) and a surface burst

with a scaled HOB $\approx$0.75 m/KT$^{1/3}$ (N130224). We did not have sufficient time or resources to develop the capability to field a buried EPEC shot where the halfraum target would be beneath the surface of our geological surrogate.

Another difference between a nuclear and a chemical HE explosion is the presence of ionizing radiation that deposits in and heats local media, causing follow-on effects to material properties. We have evidence of clearly separated x-ray and blast effects in the ground surrogate in the second EPEC data shot (N130210). These phenomena are amenable to modeling – one can calculate the energy transport/deposition/reflection etc. with one type of code, and use the pre-formed state of the ground or atmosphere as input for a different type of model, such as the GEODYN code used in this work. In principle, such first-principles models can be predictive of many radiation-driven observations to date (examples are found in Glasstone and Dolan). Once such modeling tools are in place, one can use NIF to perform experimental validations. The laser-driven target produces x rays, and simulations to date show rich and potentially useful time-dependent phenomena in the x-ray-atmosphere interaction that might be useful to measure in order to determine how x-ray energy modifies material properties that, in turn, influence acoustic energy signatures.

[1] E. I. Moses, R. E. Bonanno, C. A. Haynam, R. L. Kauffman, B. J. MacGowan, and R. W. Patterson Jr, Eur. Phys. J. D **44**, 215 (2007).

[2] C. A. Haynam, P. J. Wegner, J. M. Auerbach, M. W. Bowers, S. N. Dixit, G. V. Erbert, G. M. Heestand, M. A. Henesian, M. R. Hermann, K. S. Jancaitis, K. R. Manes, C. D. Marshall, N. C. Mehta, J. Menapace, E. Moses, J. R. Murray, M. C. Nostrand, C. D. Orth, R. Patterson, R. A. Sacks, M. J. Shaw, M. Spaeth, S. B. Sutton, W. H. Williams, C. C. Widmayer, R. K. White, S. T. Yang, and B. M. Van Wonterghem, Applied Optics **46**, 3276 (2007).

[3] D. Ryutov, R. P. Drake, J. Kane, E. Liang, B. A. Remington, and W. M. Wood-Vasey, Astrophys. J. **518**, 821 (1999).

[4] K. D. Koper, T. C. Wallace, R. E. Reinke, and J. A. Leverette, Bull. Seis. Soc. Amer. **92**, 527 (2002).

[5] S. R. Ford, A. J. Rodgers, H. Xu, D. C. Templeton, P. Harben, W. Foxall, and R. E. Reinke, Bull. Seis. Soc. Amer. **104**, 608 (2014).

[6] J. Grun, J. Stamper, C. Manka, J. Resnick, R. Burris, and B. H. Ripin, Appl. Phys. Lett. **59**, 246 (1991).

[7] G. F. Kinney and K. J. Graham, *Explosive Shocks in Air* (Springer-Verlag, 1985).

[8] S. Glasstone and P. J. Dolan, *The Effects of Nuclear Weapons*, 3rd ed. (United States Department of Defense and United States Department of Energy, 1977).

[9] I. Lomov, "Simulation of dense and dilute multiphase compressible flows with Eulerian-Lagrangian approach" in *Proc. of 6th International Conference on Multiphase Flow, ICMF 2007*, edited by Martin Sommerfeld (ICMF CDROM, 2007) ISBN 978-3-86010-913-7.

[10] Y. Kanarska, I. Lomov, L. Glenn, and T. Antoun, Annals of Nuclear Energy **36**, 1475 (2009).

[11] I. Lomov, R. Pember, J. Greenough, and B. Liu, "Patch-based Adaptive Mesh Refinement for Multimaterial Hydrodynamics" in *Proc. of Joint Russian-American Five-Laboratory Conference on Computational Mathematics*, edited by J. Kamm (Los Alamos National Laboratory, 2009).

[12] P. Bell, D. Lee, A. Wootton, B. Mascio, J. Kimbrough, N. Sewall, W. Hibbard, P. Dohoney, M. Landon, G. Christianson, J. Celeste, and J. Chael, Rev. Sci. Instru. **72**, 492 (2001).

[13] W. Hibbard, M. Landon, M. Vergino, F. Lee, and J. Chael, Rev. Sci. Instru. **72**, 530 (2001).

[14] R. Plummer, "Diagnostic Instrument Manipulator (DIM) upgrades for reliability and operational efficiency in a radiological contamination environment at the National Ignition Facility (NIF)" in *Target Diagnostics Physics And Engineering For Inertial Confinement Fusion II*, Proceedings of SPIE, Vol. 8850, edited by Bell, PM and Grim, GP (SPIE, 2013).

[15] E. M. Giraldez, P. B. Mirkarimi, J. A. Emig, K. B. Fournier, H. Huang, J. S. Jaquez, E. C. Losbanos, M. J. May, J. D. Sain, M. E. Schoff, N. E. Teslich, M. T. Vu, and R. J. Wallace, Fusion Science and Technology **63**, 242 (2013).

[16] M. J. May, K. B. Fournier, C. G. Brown Jr., W. H. Dunlop, J. O. Kane, P. B. Mirkarimi, J. Moody, J. R. Patterson, M. Schneider, K. Widmann, and E. Giraldez, High Energy Density Physics **11**, 45 (2014).

[17] H. Huang *et al.*, Fusion Science and Technology **51**, 519 (2007).

[18] E. L. Dewald, K. M. Campbell, R. E. Turner, J. P. Holder, O. L. Landen, S. H. Glenzer, R. L. Kauffman, L. J. Suter, M. Landon, M. Rhodes, and D. Lee, Rev. Sci. Instrum. **75**, 3759 (2004).

[19] K. M. Campbell, F. A. Weber, E. L. Dewald, S. H. Glenzer, O. L. Landen, R. E. Turner, and P. A. Waide, Rev. Sci. Instrum. **75**, 3768 (2004).

[20] W. L. Kruer, *The Physics of Laser Plasma Interactions* (Westview Press, 2003).

[21] D. J. Strozzi, E. A. Williams, D. E. Hinkel, D. H. Froula, R. A. London, and D. A. Callahan, Phys. Plasmas **15**, 102703 (2008).

[22] D. H. Froula, D. Bower, M. Chrisp, S. Grace, J. H. Kamperschroer, T. M. Kelleher, R. K. Kirkwood, B. MacGowan, T. McCarville, N. Sewall, F. Y. Shimamoto, S. J. Shiromizu, B. Young, and S. H. Glenzer, Rev. Sci. Instrum. **75**, 4168 (2004).

[23] A. J. Mackinnon, T. McCarville, K. Piston, C. Niemann, G. Jones, I. Reinbachs, R. Costa, J. Celeste, G. Holtmeier, R. Griffith, R. Kirkwood, B. MacGowan, S. H. Glenzer, and M. R. Latta, Rev. Sci. Instrum. **75**, 4183 (2004).

[24] S. Dixit, M. Feit, M. Perry, and H. Powell, Optics Letters **21**, 1715 (1996).

[25] C. Brooksby and C. Smith, "Mechanical Engineering Safety Note EPEC Assembly on DIM (NIF document MESN10-000077-AB)," (2013).

[26] N. Shingleton, D. Kalantar, R. Wood, T. McCarville, J. Klingmann, and A. Manuel, "Alignment of an X-Ray Imager Line of Sight in the National Ignition Facility (NIF) Target Chamber using a Diagnostic Instrument Manipulator (DIM) and Opposed Port Alignment System (OPAS)" in *Target Diagnostics Physics And Engineering For Inertial Confinement Fusion*, Proceedings of SPIE, Vol. 8505, edited by Bell, P and Grim, GP (SPIE, 2012).

[27] J. O. Kane, C. A. Brooksby, C. G. Brown, S. M. Compton, W. H. Dunlop, K. B. Fournier, I. N. Lomov, N. D. Masters, M. J. May, P. B. Mirkarimi, H. A. Scott, D. J. Strozzi, O. Y. Vorobiev, G. B. Zimmerman, R. Guyton, E. J. Huffman, and E. A. Smith, "Design of the Energy Partitioning Energy Coupling (EPEC) NIF Experiment, LLNL technical report LLNL-TR-636734," (2013).

[28] L. M. Lee, D. E. Johnson, F. Bauer, R. P. Reed, and J. I. Greenwoll, "Piezoelectric Polymer PVDF Application Under Soft

X-Ray Induced Shock Loading" in *Shock Compression of Condensed Matter 1991*, edited by S. Schmidt, R. Dick, J. Forbes, and D. Tasker (Elsevier Science Publishers B.V., 1992).

[29] R. A. Graham, F. W. Neilson, and W. B. Benedick, J. Appl. Phys. **36**, 1775 (1965).

[30] Eric A. Smith, EPEC Air Blast Shock Sensors Qualification Tests - PVDF Gauge Shock Tube Function Testing Preliminary Report, Ktech Report K2057, September 2011; Charles G. Brown Jr., Ktech Airblast Sensor Signal Estimation, 15 November 2011 (unpublished).

[31] C. G. Brown Jr., E. Bond, T. Clancy, S. Dangi, D. C. Eder, W. Ferguson, J. Kimbrough, and A. Throop, Journal of Physics: Conference Series **244**, 032001 (2010).

[32] A. Horn, E. W. Kreutz, and P. R., Appl. Phys. A **79**, 923 (2004).

[33] W. M. Adams, R. G. Preston, P. L. Flanders, D. C. Sachs, and W. R. Perret, J. Geophys. Res. **66**, 903 (1961).

[34] J. R. Murphy and J. A. Lahoud, Bull. Seis. Soc. Amer. **59**, 2325 (1969).

[35] Henry F. Cooper Jr., "Empirical Studies of Ground Shock and Strong Motions in Rock, DNA 3245," (Oct. 1973), R&D Associates, Defense Nuclear Agency, Washington, D.C.

[36] J. L. Drake, S. E. Blouin, and E. B. Smith, "Ground Shock Beneath Near-Surface Explosions: The DUG Methodology," (Nov. 1988), Applied Research Associates, Defense Nuclear Agency, Washington, D.C.